DEMONSTRATION OF HIGH POROSITY COOLING SYSTEMS USING NOVEL THERMOCHROMIC LIQUID CRYSTAL METHOD

A.Wambersie – P.T. Ireland

Department of Engineering Science, University of Oxford
Oxford OX1 3PJ, UK
Email: augustin.wambersie@eng.ox.ac.uk

ABSTRACT

High porosity cooling systems have recently shown promise as a potential option for increasing turbine blade cooling effectiveness. To demonstrate the viability of this approach, a set of turbine blades with a double wall high porosity cooling scheme was manufactured from engine-grade materials. These were tested for metal effectiveness at steady state using a low-temperature high-speed cascade with engine-representative conditions.

Metal effectiveness values were obtained using a novel post-processing technique, based on the response of multiple narrow-band liquid crystals allowing for high-resolution in situ measurements.

Results demonstrated the high cooling potential of such designs as well as their potential implementation within a double-walled system. The comparison between the measured metal effectiveness values to existing state of the art cooling designs suggests that the potential increase in cooling effectiveness exceeds 5-7% at existing mass flows or alternatively, allows for a 15-20% reduction in coolant mass flow for equivalent cooling effectiveness levels.

KEYWORDS

METAL EFFECTIVENESS, TRANSPIRATION COOLING, HIGH POROSITY, DOUBLE WALL COOLING, TLCS

NOMENCLATURE

BR	Blowing ratio
D	Film hole diameter (mm)
h	heat transfer coefficient (HTC) (W/m^2.K)
i	Pixel relative intensity
k	Metal Conductivity (W/m.K)
L	Pressure surface length (mm)
M*	nondimensional mass flow rate
$\dot{m}_c$	Coolant mass flow rate
PR	Pressure Ratio
W_c	Coolant mass fraction
s	Streamwise distance (mm)
x	Spanwise distance (mm)
ε_m	Metal Effectiveness

INTRODUCTION

The ever-increasing demands of turbine inlet temperatures necessary to drive even greater engine performances have fueled research in turbine blade cooling for decades. Open porous structures integrated into the wall of high-performance turbine aerofoils have long been identified as very

Copyright © by the Author

efficient cooling systems. The ability of these structures to generate highly effective and uniform cooling films in the presence of a cross-flow has resulted in transpiration cooling being extensively tested as a solution to turbine blade cooling at a conceptual level. However, manufacturing challenges and sensitivity of these systems to flow blockage has been thought to limit their application.

Recent studies in high porosity film cooling features have demonstrated that a viable intermediate between film cooling and transpiration cooling can be implemented (Wambersie, Ireland and Mayo 2021). These designs operate at blowing ratios far below typical film designs, yet achieve much greater film effectiveness levels for the same coolant mass flow rate. The reduced blowing ratio and uniform spanwise distribution results in a significant reduction in mixing between the coolant and mainstream, minimizing the associated decay in film effectiveness. This is particularly significant on the suction surface of the blade where curvature and a favorable pressure gradient almost suppress mixing altogether. Finally, the interactions between closely packed film holes have been seen to lead to beneficial film-film interactions between counter-rotating vortex pairs, contributing to the film remaining attached to the blade surface, even at high BRs (Jiang, et al. 2017).

Obtaining experimental metal effectiveness data on a full turbine cooling system is typically a very challenging and time-consuming process, with large expensive engine scale rigs required. Alternatively, small-scale experimental facilities such as flat plates or low-temperature cascades have been used to test out various design concepts through analogous measurement techniques such as film effectiveness or HTCs. The present work addresses the gap in fidelity of conditions between these extremes by testing metal aerofoils in a cascade with representative Reynolds and Mach numbers. A similar approach is reported by Nathan et. al. (2012) who demonstrate a similar overall approach relative to this study using an NGV cascade on a traditional film-cooled geometry.

Advances in CFD offer a possible alternative route for investigating new cooling designs, however, newer high porosity cooling systems have proven difficult to accurately predict using standard modelling approaches due to the high number of individual film cooling features. Predictions have failed to progress past the flat plate stage, and struggle to manage curvature and pressure gradients. (Jiang, et al. 2017)

This paper discusses metal effectiveness data, as defined by Equation 1, obtained using an experimental setup that offers a relatively high degree of fidelity despite using straightforward pre-existing tools. T_∞, T_m and T_c refer to the mainstream, metal, and coolant temperatures respectively.

$$\boldsymbol{\varepsilon_m = \frac{T_\infty - T_m}{T_\infty - T_c}} \quad \textbf{(1)}$$

METHOD

Rig

Experiments were carried out within a high-speed, low-temperature, single-blade passage, first designed and built by Gurram et al (2016). Details of the rig and its operating conditions are described in detail by Ngetich (2019). The flow is scaled to match the Reynolds, Mach and pressure distribution of real engine conditions. This earlier setup was modified by the inclusion of a double-layer heater mesh upstream of the test section (Gillespie, Wang and Ireland 1995), which allowed for the mainstream temperature to be raised by 35K. With the coolant air being approximately 5K colder than atmospheric, a temperature difference of 40K could be developed.

The walls of the rig are fabricated from thick Perspex to allow full optical access to the blade surface. The imaging of the blade was carried out through the use of three CCD cameras as shown by Figure 1. These are positioned around the blade so that their overlapping fields of vision cover the entire blade surface. Images were continuously recorded throughout the experiments in order to obtain an intensity history for each pixel. The coolant mass flow was measured using an orifice plate.

 Copyright © by the Author
Downloaded from www.euroturbo.eu

Thermochromic Liquid Crystals

Temperature based experiments using metal parts capture the effects of conduction, and internal and external convection when test pieces with engine representative Biot numbers are used in engine representative flows. This approach allows for a comprehensive assessment of the blade cooling performance to be evaluated, as opposed to specific film effectiveness or HTC experiments which only measure a component of the driving heat transfer mechanism.

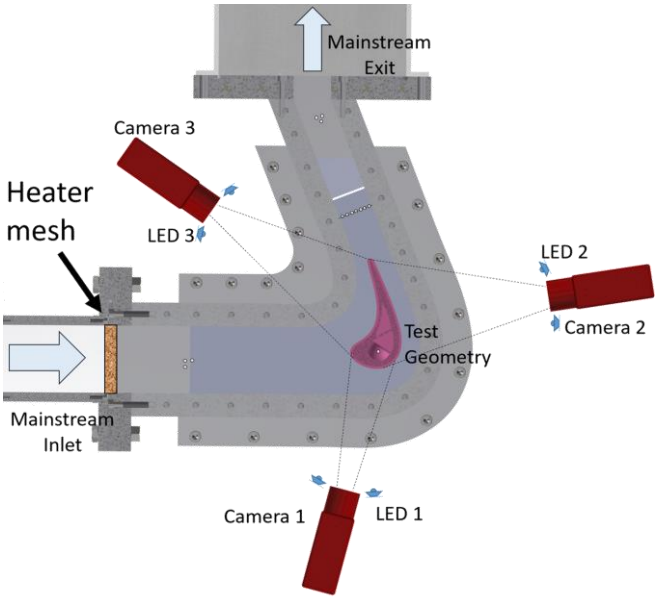

Figure 1 Schematic of the experimental facility with heater mesh

Thermochromic Liquid Crystals (TLCs) offer a non-intrusive approach to determining the metal temperature of the blade surface. TLCs are particularly suited for use in high-speed experiments as they are insensitive to variations in pressure. A comprehensive assessment of TLCs is given by Ireland et. al. (1999). In brief, they can be applied as a coating of temperature-sensitive material that becomes optically variable as a function of temperature. For this experiment, narrow-band liquid crystals were used to measure the metal surface temperature.

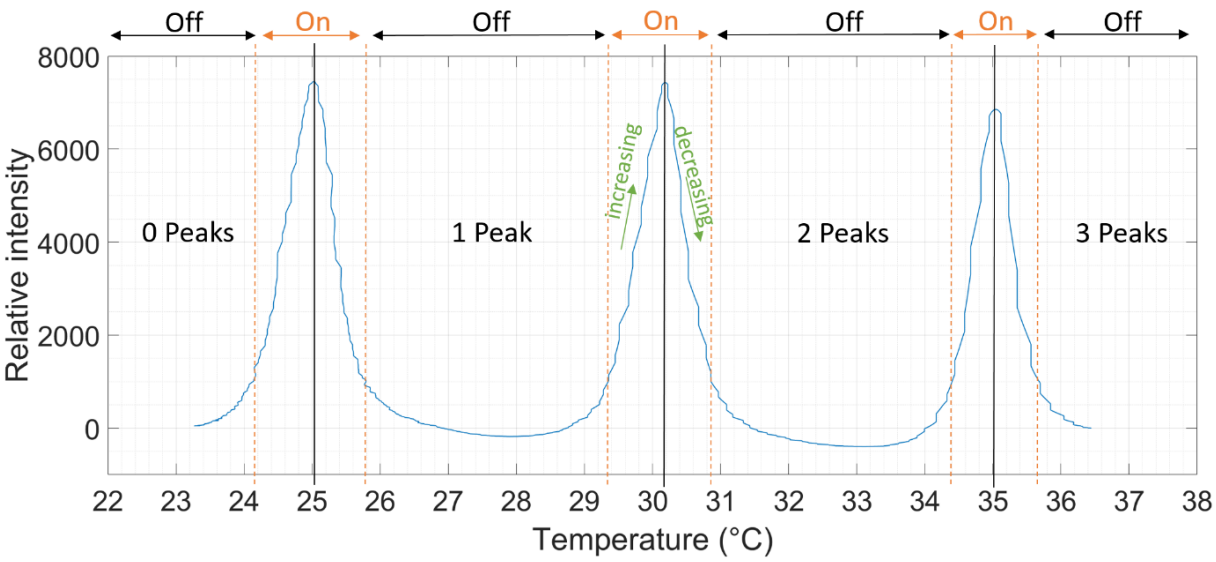

Figure 2 Example of narrowband liquid crystal response applied to test aerofoil with temperatures of principle and secondary contours shown in black and orange respectively

Copyright © by the Author

Narrowband crystals have an optically dynamic temperature range of approximately 1 degree Celsius. Within this temperature band, the reflected light intensity peaks at a specific temperature predetermined by the properties of the crystal, resulting in a color display which identifies an isothermal surface region. The benefit of this approach is that, while the temperature data obtained is not continuous, the confidence of this data is significantly higher than wideband or infrared methods. Narrow band crystals also have much lower surface orientation dependency than wide band crystals which is crucial on a 3D geometry. A similar experimental approach is taken by Ryley et. al (2019) who recommend viewing angles kept within 70° to avoid intensity orientation dependency. Other authors indicate that hue sensitivity is minimal below viewing angles of 45° (Kakade, et al. 2009). In the present work at all locations of the blade have view angles below 50° through the use of three cameras with overlapping fields of view, with the exception of the leading edge where the viewing angle approaches 70°.

Three different liquid crystals were combined to enable multiple temperature contours to be visualized. Figure 2 shows an in-situ measurement of the light intensity response of the TLCs used in this investigation achieved using a surface thermocouple. The liquid crystals were chosen with peaks at approximately 25°C, 30°C, and 35°C. By using 3 crystal bands, three contours, indicated by the black vertical lines in Figure 2 could be established, resulting in 4 distinct temperature bands. To improve the signal to noise ratio, a combination of warm light with a color temperature of 3000K and green filter with a transmission wavelength of 550nm were added to the lenses.

Light intensity values at each pixel are first subtracted from a reference image taken when the test pieces are cold and at a uniform temperature below the temperature-sensing range of the TLC coating. These processed images are then normalized by the maximum intensity achievable by each pixel.

As the three different temperature sensing crystals produced almost identical signals, the different signal peaks had to be systematically discerned by making use of the intensity history of each pixel. During experiments, the mainstream and coolant flow were turned on first and then the mesh was slowly warmed up until the blade reached its steady state temperature distribution. Steady state conditions were monitored by a single surface thermocouple left on the blade during tests and experiments were run well past this value had stabilized.

By starting with the entire blade at a temperature below the measurable temperature range, each pixel transitioned through a different number of identifiable temperatures, dependent on the final steady-state temperature achieved. A peak finding algorithm could be applied to the intensity history of each pixel in order to count the number of peaks that had been passed. An example of a pixel intensity history is shown in Figure 3, where the individual peaks of the 25°C and 30°C are identified.

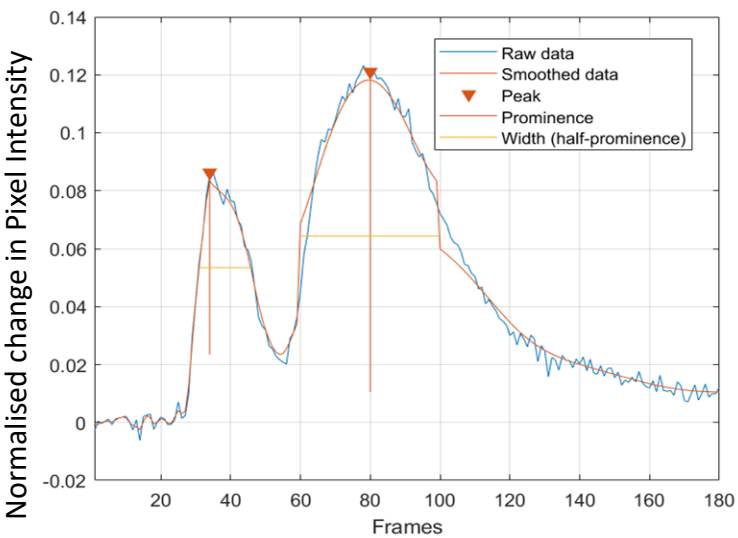

Figure 3 Example of signal response of a pixel between 30.9 and 34.4℃

Copyright © by the Author

Once sufficient signal strength and image quality was established, additional contour lines could be added around the intensity peaks. By establishing a cut-off relative signal intensity at which the crystal is deemed "on" or "off", three more temperature bands could be created. These are indicated in Figure 2 by the vertical orange dotted lines and were chosen to be at a relative pixel intensity of 0.02, approximately 0.5 degrees on either side of the intensity peaks. These values were selected as the gradient of the crystal temperature-intensity graph remained steep enough to infer values with meaningful confidence intervals. Whilst this results in contours bands of uneven width, the additional temperature levels provide extra data which yields further insight when large portions of the blade are close to the critical TLC temperatures. Finally, the additional three "on" bands can further be divided into two. As the crystal intensity history is known, it can be determined from the derivative of the pixel intensity-time plot whether the pixel is moving towards or away from an intensity peak. This results in 9 temperature contours and 10 separate temperature bands being established from the use of only 3 crystals.

Uncertainty analysis

The experimental uncertainty in metal effectiveness can be calculated for each isothermal contour line. In this analysis, the perturbation method described by Moffat (1988) is used. These uncertainties stem from the measurements of mainstream, coolant, and crystal calibration temperatures, as well as the measurement of light intensity.

In order to simplify the uncertainty analysis for the light intensity, 6 calibration readings equivalent to Figure 2 were taken around the blade midspan at regular intervals of s/L=0.4, accounting for different orientations and illuminations. The estimated error in intensity measurements of the liquid crystal response resulted in a maximum variation in temperature of ±0.3K. This is in line with other studies quantifying the accuracy of narrow-band liquid crystals (Sabatino, et al. 2000). Thermocouple measurement errors were estimated to be ±1K once combined with the signal conditioning amplifier following in situ calibrations. Table 1 calculates the overall uncertainty to be ±0.047 or approximately 7% for a nominal metal effectiveness of 0.65. It is worth noting that the majority of the error originates from the use of conventional K type thermocouples and the relatively small temperature difference between mainstream and coolant.

Variable	Nominal Value	Measurement uncertainty	Sensitivity coef.	Normalized by Result
T_∞	318 K	1	0.013	1.97%
T_c	291 K	1	0.024	3.66%
T_{cali}	300 K	1	0.037	5.70%
$T_{crystal}$	298 K	0.3	0.037	1.71%
			Absolute error	±0.0472
			% Error of calculation	7.26%

Table 1 Calculation of errors for a nominal metal effectiveness isothermal contour of 0.65

GEOMETRY

Design

The core of the internal geometry used for the transpiration blades is taken from previous studies of double-wall effusion systems (Ngetich 2019). These systems were seen to provide good convective cooling properties but, more importantly, provided a cooling strategy that the authors could tune to direct tailored quantities of coolant to the appropriate film hole arrays also described as panels.

Copyright © by the Author
Downloaded from www.euroturbo.eu

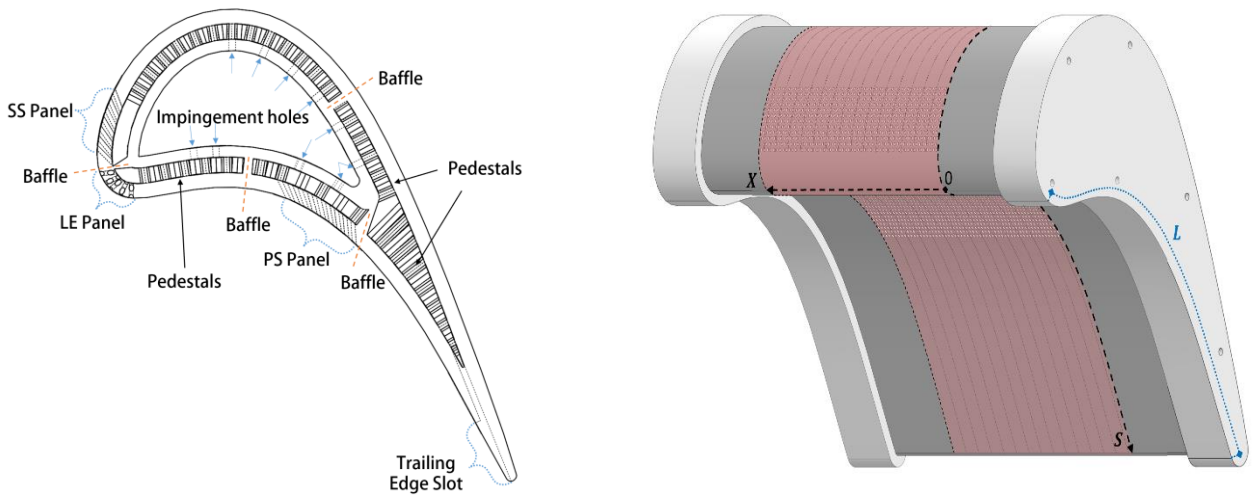

Figure 4 (a) Schematic Cross section of TP095TE and (b) blade surface coordinate system

In the double wall geometry, illustrated by Figure 4(a), the air is fed to a single inner plenum within the inner wall. The coolant is first directed through a bank of impingement holes within the inner wall. The jets formed by these holes and consequent impingement onto the outer wall contribute significantly to the internal cooling performance. The coolant then migrates through pedestal banks between the walls. The coolant finally effuses through the different arrangements of film cooling holes where it generates an effective external film. As the panels of film cooling holes operate with a relatively low-pressure margin, a wide range of feed pressures is required by the three different panels distributed around the blade. In order to mitigate excessive coolant migration, baffles are included to segment the region between the inner and outer wall. The resultant geometry has three separate cooling modules, each containing its own bank of impingement holes, pedestals, and film cooling holes.

The design point for the coolant mass flow was set at 3.5% of the overall mainstream mass flow rate. The coolant mass flow to each module was chosen to maximize the overall predicted combined film effectiveness over the entire blade. These predictions were made by interpolating and superimposing data from empirical results of individual panels at varying mass flows and blowing rates. This resulted in each panel being designed to operate at a given mass flow and mean blowing ratio (BR), with optimal BR values expected to lie between 0.3 on the suction surface and 0.4 on the pressure surface as previously determined by Wambersie et al. (2021). Combined with the discharge coefficients determined for each panel, a simple flow net model was developed. For a given inlet pressure, the mass flow and pressure ratio to each module could be set by the impingement hole diameter and number of impingement holes.

As the minimum hole diameter was identified as a potential limit to the implementation of high porosity film cooling designs at engine scales, two-hole sizes were investigated, both above and below existing manufacturing capabilities at engine scale. An additional module was included in either geometry in order to include a trailing edge slot so that the significance of such a feature could be investigated. Further information of the different geometries tested is given in Table 2.

Geometry	Film hole *D* (mm)	SS Film rows	PS Film rows	LE Film rows	TE included	Pitch/D	Impingement *D* (mm)
TP075S	0.75	7	9	5	N	2.1	1.5
TP075TE	0.75	7	9	5	Y	2.1	1.5
TP095S	0.95	5	6	3	N	2.1	1.5
TP095TE	0.95	5	6	3	Y	2.1	1.5

Table 2 List of geometries tested with information on film cooling features

Copyright © by the Author

Test Piece manufacture and rig scaling

A laser sintered additive manufacture was used to produce the intricate geometries. As the conductivity of the test piece has a significant impact on the metal effectiveness distribution and cooling performance, the Biot number of the experiment, given by Equation 2, is matched to engine conditions with blades made of CSMX-4. From the range of different materials available for AM manufacturing, Inconel 625 was selected as it resulted in a Biot number within 2.5% of the target value. Table 3 presents the values and constants used to make this assessment. The main assumption made for this calculation was that the Nusselt number of the rig would match that of the engine. This assumption is valid as by design, both engine and rig share the same Reynolds number, Mach number and Prandtl numbers.

$$Bi = \frac{h}{k} L_{wall} \tag{2}$$

To minimize any thermal conduction between the test piece and the surrounding test facility, and to eliminate the impact of end wall effects, the test pieces were held in place by uncooled supports made of high-strength ABS plastic with very low thermal conductivity. Analysis showed that the effect of heat lost to the supports had a negligible effect on the aerofoil temperature.

Whilst film hole diameters were chosen based on engine scale manufacturing capabilities, hole diameter was also a concern for manufacturing the test pieces. AM, particularly in the case of laser sintering, results in the contraction of small diameter hole features as the sintered material melts and expands into the hole void. This contraction needs to be accounted for, predominantly through trial and error as these effects are highly dependent on orientation and geometry. Figure 5 shows the AM test pieces immediately post-sintering. Measurements of the test pieces showed actual holes sizes to be between 0 and 4% oversized, as holes in the center of the lattice failed to contract as predicted due to the lower bulk density.

	Engine	**Rig**
Operating temperature (K)	2000	310
Conductivity of air (W/m.K)	0.083	0.0283
Metal material	CMSX-4	Inconel 625
Metal conductivity (W/m.K)	28 Abdul et al. (2007)	9.8
HTC (approximate) (W/m2.K)	8400	1248
Nusselt number	101.2	101.2
Wall thickness (m)	0.001	0.0023
Biot Number	0.3	0.293

Table 3 Biot Number scaling

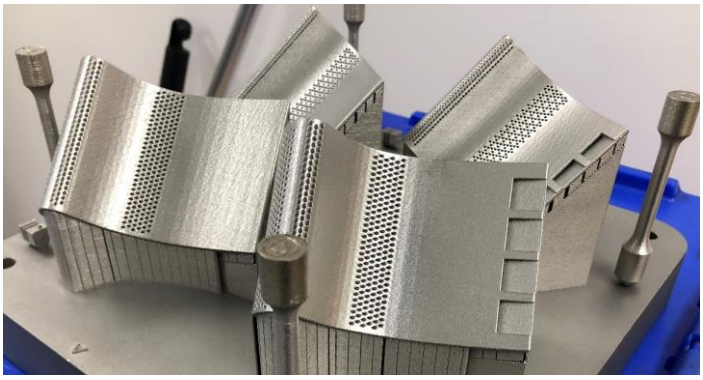

Figure 5 Test pieces as manufactured by Laser sintering AM

TLC RESULTS

The metal effectiveness contour plot of the first geometry TP075S is shown in Figure 6. The ticks and labels on the color bars indicate the values of each isothermal contour line. The color of each

 Copyright © by the Author
Downloaded from www.euroturbo.eu

contour band is taken at the mean of these two values. The plots show the leading edge at s/L=0 with the pressure surface and suction surface respectively corresponding to positive and negative values of s/L. Due to the optical constraints of taking measurements within the film holes, no values were assigned to the inside of the film holes.

At the target mass flow and above, high and consistent values of metal effectiveness are achieved from s/L = 0.6 to s/L = -1, representing just under two thirds of the entire blade surface. As expected, the suction surface panel generates a large region of highly effective coolant film, whilst films generated by the leading edge are able to cool the gap between the pressure surface panel. Observations made during the transient warmup period before reaching steady state confirm that the internal impingement holes, particularly those feeding the leading edge and suction surface at s/L=0.2 and s/L=-0.6, contribute to cooling, thereby counteracting any streamwise decay in film effectiveness.

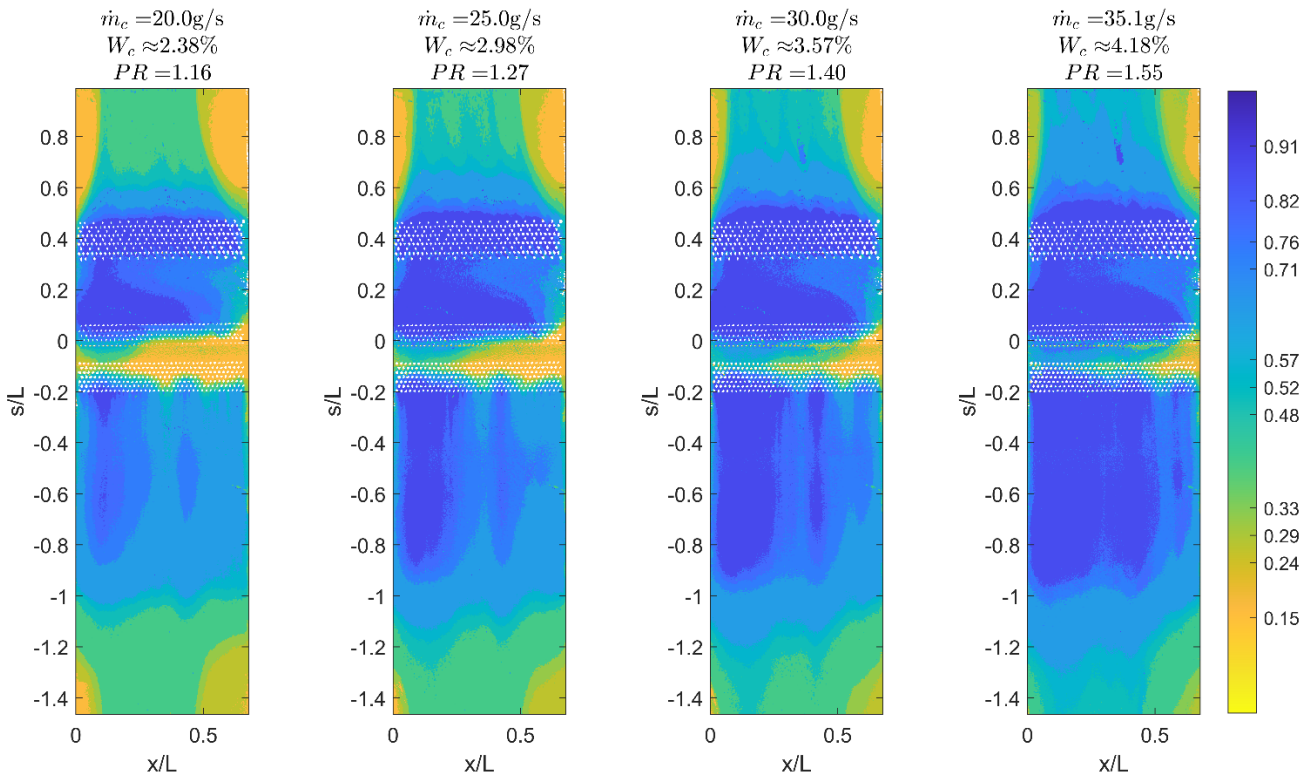

Figure 6 Metal effectiveness results for geometry TP075S

The first geometry also highlights the challenges of cooling the leading edge using a highly porous system at lower mass flows, with sections of the leading edge remaining below the threshold of the highest discernable TLC signal. However, at higher mass flows closer to the expected operating point, the leading edge is cooled to some degree. The coolant is also seen to favor the left side of the blade, with coolant entering the blade from the right-hand side of the images. This is best described by the increased loss coefficient when the inside cross flow velocity is high. A region of higher static pressure also develops opposite the coolant inlet where the internal flow stagnates. Such behavior is usually observed in manifolds with high small duct to exit area.

An unexpected phenomenon can be observed towards the trailing edge of the results, particularly on the pressure surface with a significant reduction of cooling occurring towards the spanwise edges of the test piece. While the narrowing of the film core has been observed to a limited degree in earlier film effectiveness results (Wambersie et al. 2021), the liquid crystals indicate a much more significant phenomenon. This effect can be seen to conduct through to the suction surface despite the metal effectiveness near the SS panel showing a more conventional full spanwise distribution. A possible explanation for this phenomenon is that the metal effectiveness in these

Copyright © by the Author

regions is driven by the unprotected corners of the test piece. As the HTCs of this region are relatively high, heat is conducted inward.

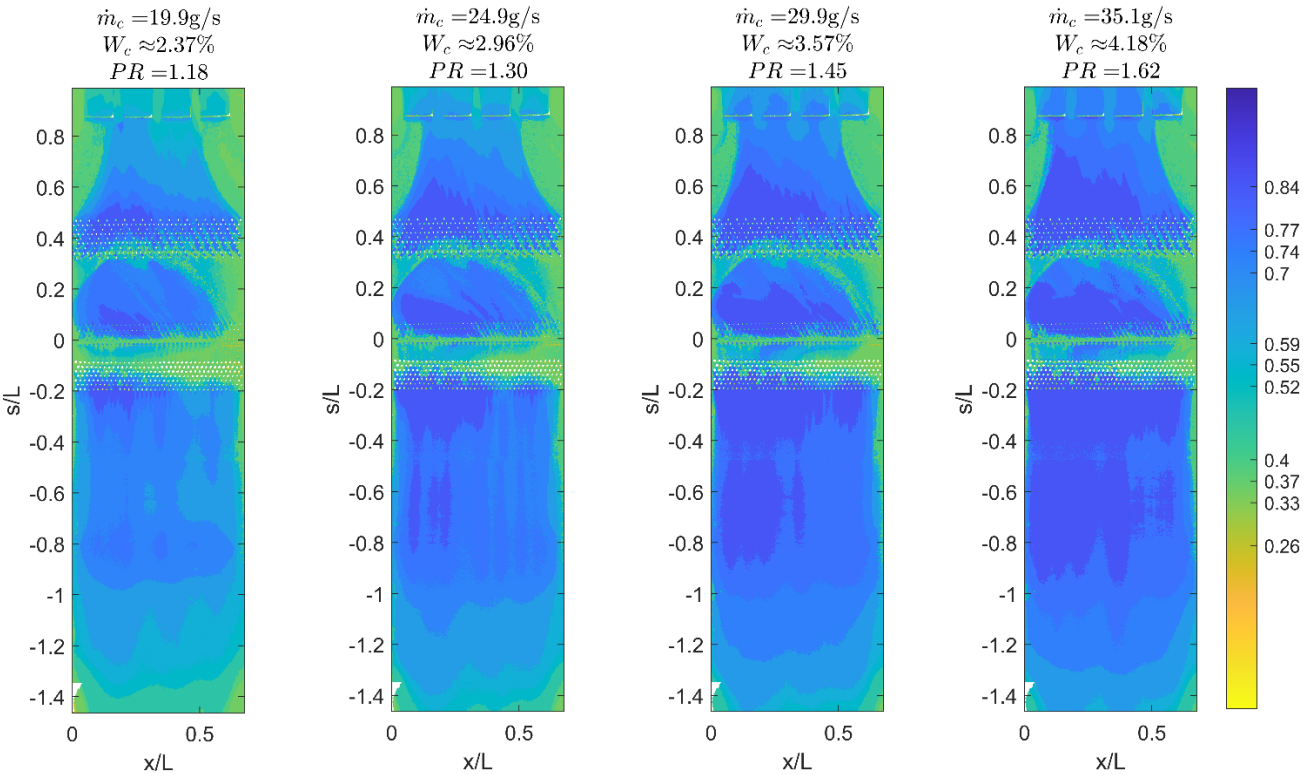

Figure 7 Metal effectiveness distribution of TP075TE

TP075TE

The addition of a trailing edge slot to geometry TP075TE results in a marked improvement in metal effectiveness towards the trailing edge on both surfaces. The addition of active cooling to the trailing edge of the blade and associated improvement demonstrates that the film effectiveness of the upstream films is not yet sufficient to passively protect the trailing edge. Improvements in TE effectiveness however come at the expense of reduced cooling towards the early suction surface and mid-pressure surface as the coolant is redirected elsewhere. It is worth noting that the positions of the metal effectiveness bands are slightly different despite indicating the same temperature due to variations in atmospheric conditions which influence the temperature of both mainstream and coolant air.

TP095TE

Increasing the hole size by slightly over 25% to 0.95mm results in an increase in metal effectiveness around the entire blade. While contrary to expectations, the geometry with larger holes and trailing edge is able to maintain larger regions of the blade at or above the maximum measurable temperature band, equating to metal effectiveness levels above 0.86. The slight variation in pressure surface panels may offer some explanation for the different cooling performances, however, this is more likely due to manufacturing challenges associated with the internal blade features leading to uneven coolant distributions throughout the blade. Variations in feed pressure ratios demonstrate how significant these variations can be, with a reduction of up to 0.24 in PR despite the geometries remaining geometrically very similar.

Copyright © by the Author

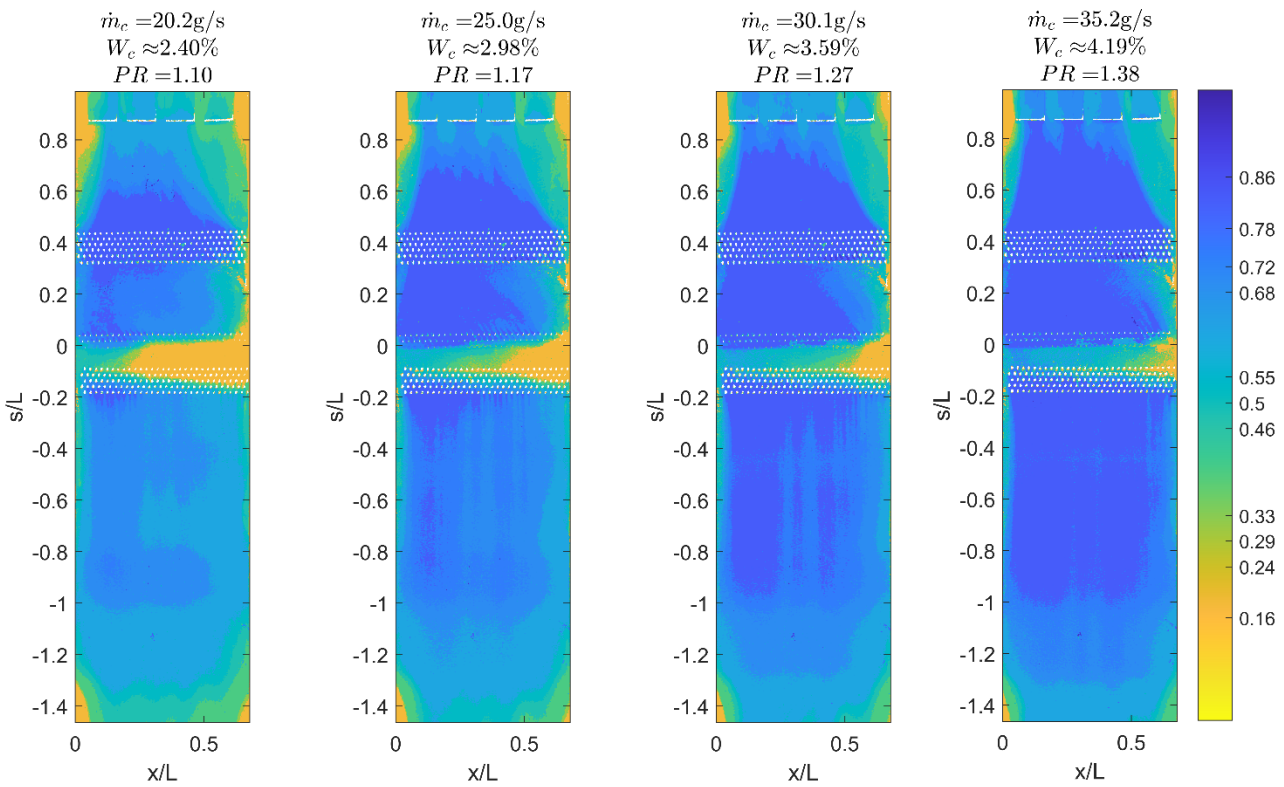

Figure 8 Metal effectiveness distribution of TP095TE

Metal Effectiveness summary plots

As previously mentioned, one of the limitations of the contour plots created using narrow-band liquid crystals is the inability to take accurate numerical linear and area averages. However, by assigning each contour its median value, a qualified average can be determined. This method is best used as a comparative tool in between test pieces as the fraction of each blade's surface area within a certain metal effectiveness range is still of critical importance to cooling system designs. The average metal effectiveness of several different regions of interest can be taken in order to compare the cooling performances. Averages of the trailing edge region, leading edge region, suction surface, and pressure surface are shown in Figure 9.

Data for the trailing edge region was taken between s/L = 0.9 and s/L = 1 which equates to approximately two-thirds of the trailing edge slots. For the leading-edge region, an average was taken over the cylindrical portion of the blade, equating to the region between s/L = -0.05 and s/L = 0.05. For the pressure surface and suction surface, an average was taken from the leading edge to the trailing edge along the respective surfaces.

Average cooling effectiveness was also calculated for the entire blade surface and plotted in Figure 10. These values are plotted against the non-dimensional mass flow m* defined by Equation 3 allowing for comparisons between test conditions and geometries.

Reference lines for theoretical internally cooled blades at different internal convective efficiencies are also included as defined by Holland and Thake (1980) and Equation 4.

$$\boldsymbol{m^*} = \frac{\dot{m}c_p}{hA} \tag{3}$$

$$\boldsymbol{\varepsilon_m} = \frac{\eta_c m^*}{1+\eta_c m^*} \tag{4}$$

Copyright © by the Author

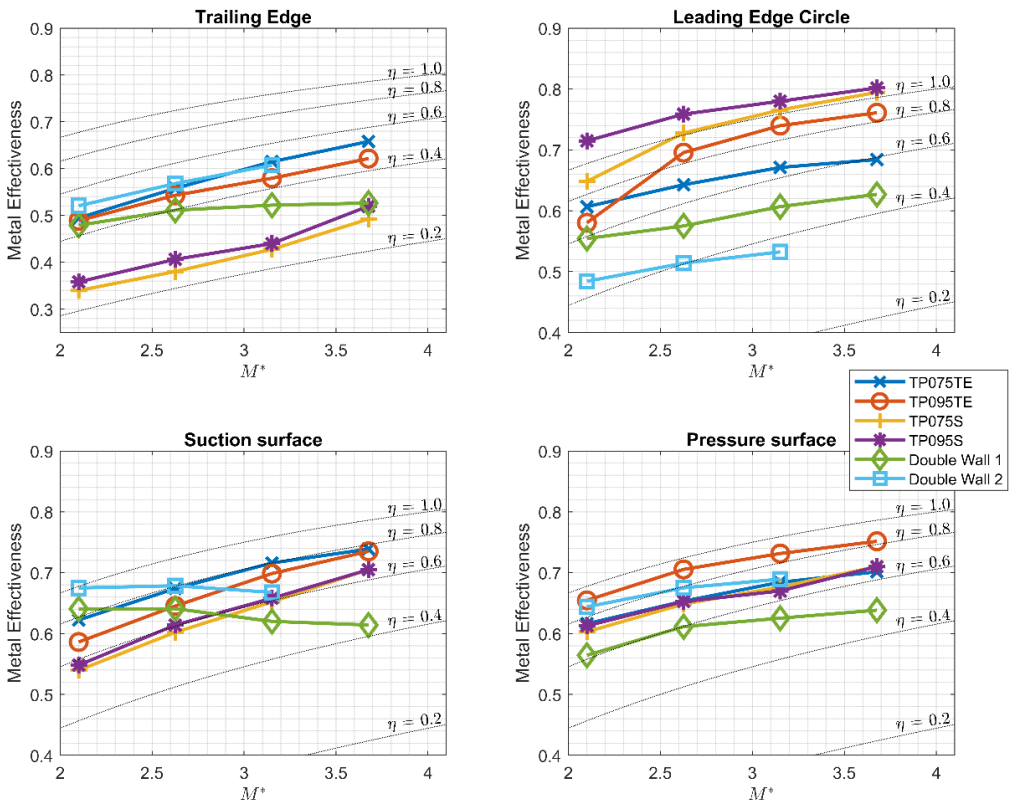

Figure 9 Mean metal effectiveness values for leading edge, trailing edge, suction and pressure surfaces

Results from the current experiment are plotted alongside previous double wall systems taken from Ngetich (2019) and tested in the same manner.

When examining the trailing edge metal effectiveness, the geometries without trailing edge slots show values at least 0.15 below those with slots. In part, this is driven by the significant edge effects that can be seen in the metal effectiveness contour plots. However, it can be noted that the cooling effectiveness of these geometries closely matches the film effectiveness levels examined for the pressure surface panels at moderate mass flow rates (Wambersie et al. 2021). Despite the metal effectiveness on the equivalent section of the suction surface being much higher, this does not appear to be sufficient to drive the metal temperature on the pressure surface.

The four geometries with trailing edge slots: the two transpiration geometries as well as the two Double Wall geometries, share a similar trailing edge metal effectiveness level at lower mass flows. As the mass flow is increased, the trailing edge metal effectiveness levels begins to diverge as coolant is fed to different upstream cooling features in varying amounts.

For the leading edge section of the blade, the results are almost inverted. For the geometries without the trailing edge slot, mass flow to the leading edge panel is increased. This panel, when not ingesting provides very high metal effectiveness. Interestingly, the two geometries with the 0.95mm film holes perform better relative to their 0.75mm counterparts despite having a reduced internal surface area. This is likely due to an increased mass flow to this section of the blade for these two geometries due to inconsistencies in internal features.

TP075TE performs the worst relative to all the transpiration designs predominantly due to the low mass flow rate of the leading edge panel which can be seen to affect the entire early pressure surface.

On the suction surface, the transpiration-cooled panel geometries result in very high effectiveness levels downstream of the panels, particularly when the internal impingement cooling is able to offset film decay. In contrast to the low porosity effusion systems, the transpiration panels can avoid film lift-off due to the interactions between films.

Copyright © by the Author

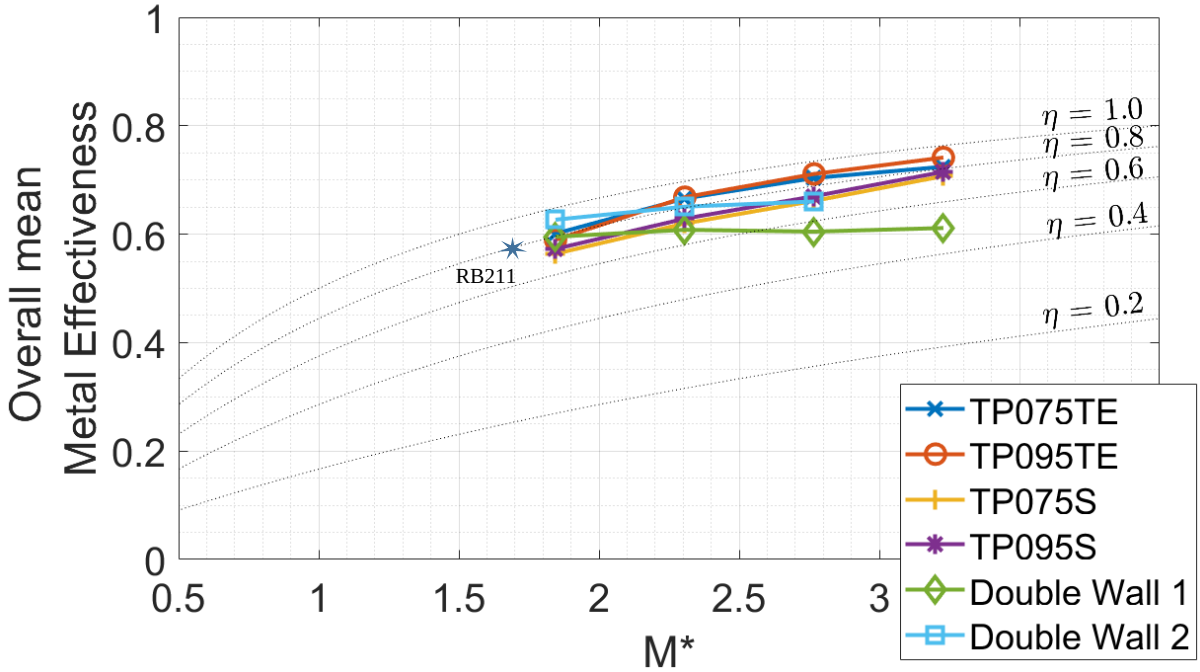

Figure 10 Mean metal effectiveness values for the entire blade surface with data taken from Holland and Thake (1980)

When examining the overall cooling effectiveness, the geometries with cooling panels and trailing edge slots can be seen to perform the best, even with large parts of the test blade's cooling performance being under-reported by the liquid crystal method. The metal effectiveness of these blades is equivalent to a theoretical blade with an internal convective cooling effectiveness of 0.8. These can achieve much higher metal effectiveness values as the film effectiveness continues to increase significantly at higher mass flow rates. By comparison, the effusion cooling systems perform relatively better at lower mass flow rates but have a very shallow gradient due to the limited film effectiveness mainly due to film lift-off. Unfortunately, very little real engine data exists in the public domain to serve as a comparison.

CONCLUSION

By combining multiple narrow-band TLCs, a detailed yet reliable surface temperature contour map could be developed. The experimental setup allowed for signal quality to be sufficiently high enough for additional temperature sub-bands to be included in the analysis. Improvements to the method would target increasing the number of bands to add further resolution to the temperature scale. Alternatively, power to the heating element could be varied to produce a range of higher inlet temperatures, with different contours stemming from various inlet temperatures being overlaid.

Most importantly, results from the double wall high porosity geometries indicate that the systems offer a highly effective film cooling design with mean metal effectiveness values exceeding 0.7 at realistic mass flow rates. Matching or exceeding the cooling capabilities of existing designs is made more significant by the relatively low maturity of these designs. Significant improvements are there to be made by refining the designs, particularly with regards to ingestion occurring at the leading edge, as well as spanwise distribution near the trailing edge. Finally, showcasing these results validates previous work on high porosity film cooling features and justifies further investigation into the matter.

Copyright © by the Author

ACKNOWLEDGMENTS

The authors wish to express their thanks for the ongoing support provided by both Rolls-Royce PLC and the EPSRC. The authors would also like to thank the technicians at the Oxford Thermofluids Institute for their assistance in the manufacturing of the experimental setup.

REFERENCES

Abdul, Abas, R., M. Hayashi, and S. Seetharaman. 2007. "Thermal Diffusivity Measurements of CMSX-4 Alloy by the Laser-Flash Method." *Int. J. of Thermophysics Vol. 28 No. 1.*

Albert, Jason E., David G. Bogard, and Frank Cunha. 2004. "Adiabatic and Overall Effectiveness for a Film cooled blade." *Proceedings of ASME Turbo Expo 2004 Power for Land, Sea, and Air.* Vienna Austria: ASME.

Gillespie, D.R.H., Z. Wang, and P.T. Ireland. 1995. Heating Element. Patent British Patent Application PCT/GB96/2017.

Gurram, Niharika, Peter Ireland, Holt Wong, and Kevin P. Self. 2016. "Study of film cooling in the trailing edge region of a turbine rotor blade in high speed flow using PSP." *Proceedings of the ASME Turbo Expo 2016: Turbomachinery Technical Conference and Exposition. Volume 5C: Heat Transfer.* Seoul, South Korea.: V05CT19A023. ASME.

Holland, M. J., and T. F. Thake. 1980. "Rotor Blade Cooling in High Pressure Turbines." *J. Aircraft AIAA Vol. 17, No.6* 412-418.

Ireland, P. T, A. J. Neely, D. R. H. Gillespie, and A. J. and Robertson. 1999. "Turbulent Heat Transfer Measurements Using Liquid Crystals." *Int. J. Heat Fluid Flow 20* pp. 355–367.

Jiang, Y, L Capone, P Ireland, and E. Romero. 2017. " "A Detailed Study of the Interaction Between Two Rows of Cooling Holes."." *Proceedings of the ASME Turbo Expo 2017: Turbomachinery Technical Conference and Exposition. Volume 5A: Heat Transfer. Charlotte, North Carolina, USA. June 26–30, 2017. V05AT12A009. ASME.*

Kakade, V.U., G.D. Lock, M. Wilson, J.M Owen, and Mayhew J.E. 2009. "Accurate heat transfer measurements using thermochromic liquid crystal. Part 1: Calibration and characteristics of crystals." *International Journal of Heat and Fluid Flow* 939-949.

Moffat, R. J. 1988. "Describing the uncertainties in experimental result." *Experimental Thermal and Fluid Science* 1 (1): 3-17.

Nathan, Marc L., Thomas E. Dyson, David G. Bogard, and Sean D. Bradshaw. 2012. "Adiabatic and Overall Effectiveness for the Showerhead Film Cooling of a Turbine Vane." *Proceedings of ASME Turbo Expo GT2012.* Copenhagen Denmark.

Ngetich, Gladys. 2019. "Study of film cooling effectiveness on a double walled effusion cooled turbine blade in a high speed flow using pressure sensative paint." *Proceedings of the ASME Turbo Expo 2019: Turbomachinery Technical Conference and Exposition. Volume 5B: Heat Transfer.* Phoenix, Arizona, USA: V05BT19A008. ASME.

Ryley, Joshua, Matt McGilvray, and David Gillespie. 2019. "Heat Transfer Coefficient Determination on 3D Geometries from Transient Thermochromic Liquid Crystal Experiments." *Journal of Thermophysics and Heat Transfer* 33:4, 1132-1141.

Sabatino, D. R., T. J. Praisner, C. R. Smith, and ab. 2000. "A high-accuracy calibration technique for thermochromic liquid crystal temperature measurements." *Experiments in Fluids* vol. 28, no. 6,: pp. 497–505.

 Copyright © by the Author
Downloaded from www.euroturbo.eu

Saul, A. J., P. T. Ireland, J. D. Coull, T. H. Wong, H. Li, and E. Romero. 2019. "An Experimental Investigation of Adiabatic Film Cooling Effectiveness and Heat Transfer Coefficient on a Transonic Squealer Tip." *ASME. J. Turbomach* 141(9): 091005.

Wambersie, Augustin, Peter Ireland, and Ignacio Mayo. 2021. "Experiments of Transpiration Cooling Inspired Panel Cooling on a Turbine Blade Yielding Film Effectiveness Levels over 95%." *Int. J. Turbomach. Propuls. Power* 6(2), 16.

Wong, T.H., P.T. Ireland, and K.P. Self. 2016. "Film Cooling Effectiveness Downstream of Trailing Edge Slots Including Cutback Surface Protuberances." *Int. J. Turbomach. Propuls. Power* 1, 4. https://doi.org/10.3390/ijtpp1010004.

Copyright © by the Author